

# A computational design method for bio-mimicked horizontal axis tidal turbines

Kulkarni, S, Chapman, C, Shah, H & Edwards, D

**Author post-print (accepted) deposited by Coventry University's Repository**

**Original citation & hyperlink:**

Kulkarni, S, Chapman, C, Shah, H & Edwards, D 2018, 'A computational design method for bio-mimicked horizontal axis tidal turbines' *International Journal of Building Pathology and Adaptation*, vol 36, no. 2, pp. 188-209

<https://dx.doi.org/10.1108/IJBPA-06-2017-0029>

DOI [10.1108/IJBPA-06-2017-0029](https://dx.doi.org/10.1108/IJBPA-06-2017-0029)

ESSN 2398-4708

Publisher: Emerald

**Copyright © and Moral Rights are retained by the author(s) and/ or other copyright owners. A copy can be downloaded for personal non-commercial research or study, without prior permission or charge. This item cannot be reproduced or quoted extensively from without first obtaining permission in writing from the copyright holder(s). The content must not be changed in any way or sold commercially in any format or medium without the formal permission of the copyright holders.**

**This document is the author's post-print version, incorporating any revisions agreed during the peer-review process. Some differences between the published version and this version may remain and you are advised to consult the published version if you wish to cite from it.**

# A computational design method for horizontal axis tidal turbines

## ABSTRACT

**Purpose:** A comparative analysis between a straight blade (SB) and a curved caudal-fin tidal turbine blade (CB) is conducted and includes an examination of aspects relating to geometry, turbulence modelling, non-dimensional forces lift and power coefficients.

**Design/ methodology/ approach:** The comparison utilizes results obtained from a default horizontal axis tidal turbine with turbine models available from the literature. A computational design method was then developed and implemented for 'horizontal axis tidal turbine blade'. Computational fluid dynamics (CFD) results for the blade design are presented in terms of lift coefficient distribution at mid-height blades, power coefficients and blade surface pressure distributions. Moving the CB back towards the SB ensures that the total blade height stays constant for all geometries. A 3D mesh independency study of a 'straight blade horizontal axis tidal turbine blade' modelled using CFD was carried out. The grid convergence study was produced by employing two turbulence models, the standard k- $\epsilon$  model and Shear Stress Transport (SST) in ANSYS CFX. Three parameters were investigated: mesh resolution, turbulence model, and power coefficient in the initial CFD, analysis.

**Findings:** It was found that the mesh resolution and the turbulence model affect the power coefficient results. The power coefficients obtained from the standard k- $\epsilon$  model are 15% to 20% lower than the accuracy of the SST model. Further analysis was performed on both the designed blades using ANSYS CFX and SST turbulence model. The variation in pressure distributions yields to the varying lift coefficient distribution across blade spans. The lift coefficient reached its peak between 0.75 to 0.8 of the blade span where the total lift accelerates with increasing pressure before drastically dropping down at 0.9 onwards due to the escalating rotational velocity of the blades.

**Originality:** The work presents a computational design methodological approach that is entirely original. While this numerical method has proven to be accurate and robust for many traditional tidal turbines, it has now been verified further for CB tidal turbines.

## KEYWORDS:

Bio-mimicry, Direct Design Method, Horizontal Axis Tidal Turbine, Tidal Energy, Comparative analysis.

## INTRODUCTION

Tidal energy is a renewable electricity source that converts the kinetic energy of moving water into mechanical power to drive generators (Shi *et al.*, 2015). This renewable source has minimal CO<sub>2</sub> emissions and is one of the many sources to address concerns over climate change (Tedds *et al.*, 2014). Horizontal axis tidal turbines (HATT) (also known as axial flow turbines) have the rotational axis parallel to the tidal flow and operate in only one flow direction. The mechanical components and principle of HATT operation is similar to the horizontal axis wind turbine (HAWT) – that is, blades are fitted to the hub, a generator converts kinetic energy from the water to mechanical energy, a shaft produces power and a gearbox drives a motor (Bai *et al.*, 2016).

There have been many advances in the development of the computational power and computational fluid dynamics (CFD) models to simulate the complex flow around the turbine (Malki *et al.*, 2014). Several studies conducted in tidal energy have examined the flow effects around turbines (Divett *et al.*, 2013; Funke *et al.*, 2014; Harrison *et al.*, 2010; Blackmore *et al.*, 2016). For example, the characteristics of a 10m diameter three-bladed HATT and the mesh was generated using ANSYS ICEM CFD (12Chord length x 20Chord length of the airfoils used in the rectangular grid); a very fine mesh near the blade wall region was used to obtain precise results but no  $y^+$  values (Goundar and Ahmed, 2013). The authors [*ibid*] found that by varying the airfoil's thickness, the blades' hydrodynamic performance and strength improved, with the rotor producing a maximum efficiency of 47.6%. Thrust and power coefficients of a 3D CFD tidal turbine model were validated with experimental data at 15° and 20° of pitch angle and synergized with the previous work of McSherry

53 *et al.*, (2011). The authors [*ibid*] analyzed the tidal turbine pressure and near-wall effects using shear  
54 stress transport (SST) model but also considered the mesh resolution and time step convergence.  
55 However, the SST model cannot capture the turbulence 3D effects as the flow passing below the  
56 turbine was not modelled by McSherry *et al.*, (2011) (Gayen and Sarkar, 2011; Boris *et al.*, 1992).  
57 Subsequently, there are higher 3D turbulence models available which have been rigorously developed  
58 and validated against flume tests (Roc *et al.*, 2013; Sescu *et al.*, 2015) but a significant drawback is  
59 the computational overhead required to solve the CFD simulation.

60  
61 A recent study by Divett *et al.*, (2016) presented a methodical numerical simulation of a large tidal  
62 turbine array. Hundreds of layouts were simulated using large eddy simulations (LES) to show the  
63 linear relationship between total power capture and its increment as additional rows are added onto  
64 turbines. The tidal cycle variation is mainly influenced by astronomical factors i.e. the sun and the  
65 moon, and the effects of salinity and temperature stratification are secondary factors (Li *et al.*, 2011).  
66 Accurately capturing the 3D turbulent flow features of the HATT requires a comprehensive  
67 understanding of the physics involved especially when experimental data is missing for validation.  
68 Experimental data is expensive to implement and hence, LES provides more flow-physics detail and  
69 places less reliance on such data by directly solving the spatially filtered Navier-Stokes equations on  
70 the larger turbulent scales (Churchfield *et al.*, 2013; Bin *et al.*, 2013; Ni *et al.*, 2013; Ciri *et al.*, 2016).

71  
72 This study develops a new computational design methodology for simulating 3D turbulent flow past  
73 straight blade (SB) and curved caudal fin blade (CB) HATTs. The design method also conducts a  
74 comparative analysis between the prototype blades designed using SST and LES-Smagorinsky  
75 turbulence models. The CFD methodology is validated against secondary data available within the  
76 literature (Goundar and Ahmed, 2013; Larwood and Zuteck, 2006). By applying this new  
77 computational design methodology, the research objective is to augment CFD simulation reliability  
78 for the CB tidal turbine blades.

## 80 **EXISTING CFD MODELLING IN TIDAL ENERGY CONVERSION**

81 Jo *et al.*, (2014) designed a horizontal axis tidal turbine based on the blade element momentum (BEM)  
82 method and calculated its efficiency performance to 40%, choosing five as the tip speed ratio. They  
83 [*ibid*] also investigated the wake distribution in the unsteady velocity flow affecting the tidal turbine  
84 system. CFD analysis was performed using a SST turbulence model and the curves of power  
85 coefficient ( $C_p$ ) and torque generated from the shaft were presented for different velocities. The  
86 airfoils were arranged in sequential order with appropriate twist angles and chord lengths to predict  
87 the tidal turbine performance using CFD to predict its torque and  $C_p$ . Kim *et al.*, (2012) analyzed a  
88 bi-directional vertical axis turbine performance in a larger area of tidal channel. Hexahedral mesh  
89 was applied in the augmentation channel and an SST turbulence model was selected. The tidal turbine  
90 blade performance was accessed based on the pressure and lift coefficients, hence demonstrating the  
91 two most significant sensitivities that cause cavitation studies at different angles of attack especially  
92 for the leading edge. Rocha *et al.*, (2014) carried out a numerical investigation and calibrated a SST  
93 turbulence model to test the operational performance of a small scale horizontal axis wind turbine  
94 (SS-HAWT). They [*ibid*] studied aerodynamic performance of the SS-HAWT based on the  
95 turbulence intensity and characteristic length ( $\beta^*$ ) to reveal the varied effects of friction over the  
96 blades.

97  
98 Afgan *et al.*, (2013) presented a comparison between Reynolds-averaged Navier-Stokes (RANS)  
99 models SST and LES numerical solutions for a three bladed HATT, validating the implemented  
100 sliding mesh technique for the unstructured mesh code over a range of tip speed ratios (TSRs). The  
101 LES solver's accuracy was tested against the optimum design condition to investigate the wake and  
102 turbine performance and highlighted issues related to simulations for high rotating velocities. Li *et*  
103 *al.*, (2013) compared three different CFD modelling approaches on a vertical axis wind turbine in  
104 higher angles of attack. The NACA 0018 SB foil was simulated using LES with a high angle of attack

105 flow. In symmetrical airfoils the stall angles appear between  $10^{\circ}$  to  $15^{\circ}$ . The authors [*ibid*] also  
106 commented on the SST turbulence model's efficacy and considered it to be assuring when simulating  
107 the adverse pressure gradients in incompressible flow. However, when SST was compared to LES,  
108 LES was computationally more challenging but produced more realistic 3D vortex diffusion and flow  
109 separation in unsteady flow computations. Force coefficients were calculated in the span wise  
110 distribution of the airfoil blades, thus proving LES as a better high fidelity CFD modelling technique.  
111 Kang *et al.*, (2012) simulated 3D turbulent flow around an axial tidal turbine, placed on the  
112 rectangular bed comprising an open channel accommodating the CFD domain to carry out LES  
113 simulations. The convoluted turbine geometry comprising rotor and stator components with moving  
114 boundaries were managed by engaging the curvilinear immersed boundary method. The CFD  
115 simulations were compared to the marine hydropower turbine using systematic grid refinement and  
116 calculating the torque sensitivity analysis. The simulations indicated that pressure fields near the  
117 turbine blades generated torque and extracted power from the water column.

118  
119 The extant literature reveals that the SST model is the most popular turbulence model used in steady  
120 state analysis of tidal turbine blades and LES for transient simulations in the absence of experimental  
121 data for validation. The literature also illustrates the need for new and alternative/ innovative  
122 methodological approaches for the CB design.

## 123 124 **A COMPUTATIONAL DESIGN METHODOLOGY**

125 The direct design method represents an optimized approach to product design that requires an  
126 understanding of the problem before collecting numerical data for analysis, validation or verification  
127 using mathematical modelling (Campi *et al.*, 2002; Shi *et al.*, 2012; Liu, 2010; Wang *et al.*, 2012;  
128 Thapar *et al.*, 2011). The direct design method begins by modelling the parametric three-dimensional  
129 SB, and then a rectangular mesh domain is generated for inputting the boundary conditions. After  
130 defining the boundary conditions, CFD analysis (as a prominent mathematical modelling technique)  
131 is performed on the tidal turbine rotors, the numerical results are compared with existing data in the  
132 literature. The final step builds the three dimensional model (Figure 1), where chosen turbulence  
133 models are tested and verified by further investigation to allow emergence of new data (Hudgins and  
134 Lavelle, 1995) The CFD results collected from the SB were comparatively analysed and evaluated  
135 with the curved caudal fin shaped blades.

136  
137 <Insert Figure 1 about here>

138  
139 The end objectives of the chosen direct blade design method were to: compare the highest power  
140 coefficient obtained for the CB with data available within tidal turbine blade literature.

## 141 142 **Design of the SB HATT**

143  
144 The SB HATT was designed in ANSYS Design Modeller (refer to Figures 2a; 2b). The airfoil  
145 considered for all the horizontal blades is a symmetrical NACA 0018. The spanwise distribution of  
146 the airfoils are stationed at every 10% of the blade whilst the distance between hub circle and the root  
147 airfoil is 20% of the total blade height.

148  
149 <Insert Figures 2a and b about here>

150  
151 The blade hub is circular and its diameter is 40% of the root airfoil chord length. The blade twist  
152 angle is higher at the root airfoil because it experiences less rotational forces and it gradually  
153 decreases across the entire span of the blade. The SB parameters are given in Table 1.

154  
155 <Insert Table 1 about here>

156  
157  
158  
159  
160  
161  
162  
163  
164  
165  
166  
167  
168  
169  
170  
171  
172  
173  
174  
175  
176  
177  
178  
179  
180  
181  
182  
183  
184  
185  
186  
187  
188  
189  
190  
191  
192  
193  
194  
195  
196  
197  
198  
199  
200  
201  
202  
203  
204  
205  
206

## **Design of the CB**

The 3D curved set of centroids defines the shape of the CB. A predictive MATLAB program was created in which the centroids of the NACA airfoil centres form a 3D shape (refer to Figure 3). The MATLAB program computes the centre of mass (gravity) for the set of airfoils used in modelling the CB.

<Insert Figure 3 about here>

The weighted centroid uses the pixel intensities in the airfoil region which weights the centroid calculation and the twist angle, which acts as the function of the incremental blade length, is further modified to create a smooth twist by fitting a third order polynomial function. The initial values of the CB NACA profile chord lengths are defined in Table 2 whilst the default profile chosen is NACA 0018.

<Insert Table 2 about here>

The X-offset and Y-offset values are used to construct the skeletal (centre line) of the CB. For programming purposes, the nearest third order polynomial regression equation on the centre line curve (refer to Figure 4) is defined as:

<Insert Figure 4 about here>

Each NACA profile centre is built on the centre line which acts as a master and each profile datum sits along its length divided by the height - the numbers of stations stay constant to reduce the computational overhead. The NACA profile sections of the curved blade are considered parallel to the x-axis, that is, the normal of each NACA section should be the y-axis. The skeleton which is fitted on the midpoint of the each airfoil has a decrease in the chord length in the blade spanwise direction which increases the surface area of the CB. The third order polynomial is fitted on the skeleton of the caudal fin centerline, starting at the airfoil root centre and passing through all the airfoil stations to the tip of the airfoil; at this end of the blade, bending occurs to create the CB. The chord lengths of the SB can be varied in linear or non-linear progression along the span-wise direction to reach the CB (refer to Figure 5).

<Insert Figure 5 about here>

### ***Strategy to Move the Curved Blade Shape Backwards to SB Shape***

The polynomial centre-line from the root chord was moved in the percentage chord lengths in order to reach the target shape. For the initial experimentation, the percentage chord lengths were moved in 0%, 25%, 50%, 75%, and 100% increments; where 0% represents the initial SB chord lengths. For convenience during experimentation, the same blade is simulated whilst the total blade height and number of stations are kept constant until the best design is found (i.e. maximum power coefficient of the blade system). The tidal turbine blade power coefficient is predominantly sensitive to total blade height but also blade twist and chord length distribution - changing the value of each and every design variable would be time consuming. To overcome this problem, repetitive transformations of the default blade design method was used. Using this approach, the percentage based chord lengths were selected and the third order polynomial function remains constant ensuring that the blade span or total blade height will replicate the default SB. Thus it was possible to define a design study strategy that moved the target shaped CB backwards to the SB shape using a linear progression function which can be demonstrated as follows:

$$T_{ASTN} = T_{SXC} \times \left( \frac{R_p}{100} \right) \quad \text{Equation 1}$$

207 Where:  $T_{ASTN}$  is the required airfoil station value;  $T_{SXC}$  is the target shape X-coordinate value for the  
 208 particular airfoil station; and  $R_p$  is the required chord length percentage. After calculating the X and  
 209 Y-offsets for the blade spinal axis variation, the backward design strategy can be plotted in Figure 6.

210  
 211 <Insert Figure 6 about here>

## 212 213 **A COMPARATIVE ANALYSIS BETWEEN THE FIVE DESIGNED PROTOTYPE BLADES**

214 Figure 7 illustrates the rectangular computational grid which was used to model the seawater domain  
 215 and the turbine disc domain, for the SB and CB geometries. The seawater domain extends five times  
 216 the turbine diameter at the inlet, ten times of the turbine diameter at the outlet whilst the height of the  
 217 rectangular grid is five times of the turbine diameter. The turbine domain was designed as a rotating  
 218 domain in CFX and then a full 360° mesh surrounding the tidal turbine blades. Figure 7 shows blade  
 219 automated meshing including the hub and tips of the SB and the CB.

220  
 221 <Insert Figure 7 about here>

### 222 223 **Mesh Independency study**

224 To establish the accuracy of the CFD solution, and to keep the computational costs low, the straight  
 225 blade was analysed using: the standard k-ε model, and SST model, at uniform  $V_{in} = 2.5\text{m/s}$ , and  $\lambda =$   
 226 5. The grid convergence study was performed by developing three different meshes: with a coarse,  
 227 medium, and fine grid for all six different meshes of the Straight Blade to predict the power, lift  
 228 coefficients, and torque on normalised mesh cells to determine how the mesh quality affects CFD  
 229 simulation results.

230 The number of nodes and the simulation time for the three cases simulated using the SST model are  
 231 highlighted in Table 3, and the three cases simulated using the standard k-ε model are given in Table  
 232 4. Table 3, and 4 summarise the key characteristics of the meshes, and it is very clear that CFD  
 233 simulation time is highly dependent on the number of mesh nodes considered. The six meshes  
 234 generated have near wall resolution i.e.  $y^+ < 10$  by using the standard wall function approach to avoid  
 235 unsatisfactory results when using the standard k – ε model.

236  
 237 <Insert Table 3 about here>

238  
 239 <Insert Table 4 about here>

240  
 241 In the case of the investigated meshes of the straight blade, the turbine domain has an increased mesh  
 242 resolution. The mesh is refined in the grids from M1 to M6 where M1, M2, M3 represent coarse,  
 243 medium, and fine mesh generated for the SST turbulence model; and M4, M5, M6 represent coarse,  
 244 medium, and fine mesh generated for the standard k-ε turbulence model. The estimated power  
 245 coefficient increased from 0.2271 to 0.4218 as shown in Figure 8.

246  
 247 <Insert Figure 8 about here>

248  
 249 It is important to note that the mesh resolution plays a pivotal role in the final CFD results. The mesh  
 250 nodes need to be small to resolve the boundary layer on the blade surfaces. The highest CP obtained  
 251 from the mesh independent study is 0.4218 for M3 from the SST model. M2 and M3 account for  
 252 nearly 1% difference in the estimated power coefficients, but the final CFD simulation time required  
 253 for convergence of the two meshes has a significant difference when the conventional mesh  
 254 independency method is employed. The power coefficients obtained from the standard k-ε model are

255 almost 15% to 20% lower than the SST model power coefficients, which is due to the poor  
256 performance of the k- $\epsilon$  model in near-wall regions and in adverse pressure gradients i.e. the fluid flow  
257 near the turbine blade surfaces; which causes the k- $\epsilon$  model to underestimate the power coefficient.  
258

259 It is clear from the final CFD simulation results that the simulation time is highly dependent on the  
260 number of mesh nodes, and the turbulence model selected. As shown in Figure 8 when using k- $\epsilon$   
261 model for all the meshes (M4, M5, and M6) employed the CFD solution under predicts power  
262 coefficient when compared with the SST model. M1 leads to the reasonable prediction of the power  
263 coefficient on the straight blade, whereas the power coefficient of M3 is slightly better than M2. Due  
264 to the slight difference, medium mesh (M2) is best regarding computational costs and is further  
265 employed for the numerical analysis carried out in the following section of the turbulence model  
266 comparison study.  
267

### 268 ***Turbulence model comparison study***

269 To understand the sensitivity of the CFD solution a consecutive study was carried out with these  
270 turbulence models at medium sized meshes. From the mesh dependency test conducted it has been  
271 found that the SST model performs superiorly in adverse pressure gradient situations than the  
272 standard k- $\epsilon$  model; because SST model is a unification of k- $\epsilon$  model and k- $\omega$  model for free stream  
273 and inner boundary layer problems respectively. Figure 9 shows the torque coefficient related to each  
274 of the two turbulence models analysed for the medium mesh. As shown in Figure 9 the SST model  
275 medium mesh has higher CM than the standard k- $\epsilon$  model in all the nine different TSR's. It can also  
276 be seen that the torque coefficient of SST medium mesh model increased by more than 25% when  
277 compared to the standard k- $\epsilon$  model medium mesh.  
278

279 <Insert Figure 9 about here>  
280

281 The highest CM is achieved at  $\lambda=5$  for both the cases, CM increases with the increasing TSR and  
282 acts as a function of TSR. It can also be noted that the non-linearity in the torque coefficient occurs  
283 after TSR of 5, and the k- $\epsilon$  model fails to capture this, due to the boundary layer and turbulence  
284 quantities to the blade wall.  
285

286 Figure 10 shows that the power coefficient increases steadily until  $\text{TSR} \approx 5$ , at which it shows the  
287 peak  $CP \approx 0.4169$  for the SST model medium mesh; after which it shows a drastic reduction with the  
288 increasing  $\lambda > 6$ . The curve for medium mesh the k- $\epsilon$  model shows that it predicts a lower power  
289 coefficient to a satisfying level of accuracy, and also under predicts the values with increasing  $\lambda$ .  
290 However, the numerical CP prediction by medium mesh the SST model observed values are  
291 approximately 20% higher than medium mesh the k- $\epsilon$  model simulation, the range  $5 \leq \lambda \leq 6$  was also  
292 validated (Bahaj et al., 2007; McSherry et al., 2011); and considered to be optimum range for HATT.  
293 The standard k- $\epsilon$  model is incapable of capturing the account of rotational forces and their effects on  
294 the turbine blades, and due to the near wall physics implementation. Thus the CP prediction by SST  
295 model is more acceptable when compared to the power coefficient predictions by the standard k- $\epsilon$   
296 model.  
297

298 <Insert Figure 10 about here>  
299

300 As a result of the mesh independency test conducted it can be concluded that the overall power  
301 coefficient shown by the SST turbulence model is more reasonable than the standard k- $\epsilon$  model, for  
302 all the cases considered. Therefore to avoid any misleading CFD results the standard k- $\epsilon$  model is not  
303 employed in any further CFD tests conducted in this research. The power coefficient of a HATT is  
304 highly sensitive to the turbulence model chosen for the CFD analysis; however the mesh independent  
305 CFD solution for SST medium mesh satisfactorily achieves the mesh independency over the SST fine

306 mesh solution which requires a massive computational overhead. Hence, the medium mesh is used to  
307 conduct the steady state analysis in following sections.

308

### 309 **Steady state CFD analysis**

310 The steady state simulations were conducted using ANSYS CFX via the SST turbulence model. In  
311 ANSYS CFX, the pressure-velocity coupling was achieved using the Rhie - Chow Option, and all the  
312 interpolation and advection values were set at high resolution. In the meshing aspect, some controls  
313 were modified to suit the concentration on the curved shaped blades because of the additional bend  
314 on the surface. Table 5 summaries the blade model functions and the respective characteristics.

315

316 <Insert Table 5 about here>

317

318 Table 3 illustrates that the number of nodes of the CB 100% case study are almost twice that of the  
319 SB case study – this is due to the flow being considerably complicated and the blade surfaces being  
320 bent for the curved blade shape. The three-dimensional modelling and steady state CFD simulations  
321 presented are conducted at constant inlet velocity of 2.5m/s, using high turbulence intensity of 10%.  
322 The outlet pressure was defined as 0bar, the blade was defined as a *rotating wall*, with no slip wall  
323 condition for mass and momentum option. The bottom and side walls were defined as free slip walls  
324 to incorporate accuracy when solving the continuity equation. The front and back walls were defined  
325 as inlet and outlet walls respectively. As the seawater flow velocity progressed over the blade pressure  
326 side, the pressure increased especially on the tip of the blade where rotational velocity was at its  
327 highest point. Figure 11 shows the comparison of the blade pressure distribution on the case studies  
328 performed (blades rotate anti-clockwise).

329

330 <Insert Figure 11 about here>

331

332 Data accompanying Figure 11 compares the steady-state pressure distribution on the five blade  
333 designs. Numerical simulations show how the seawater flow behaves on the trailing and leading edges  
334 on the pressure side of the blade. The varying lift coefficient distribution is also demonstrated by  
335 plotting the blade mid-span coefficient of lift distributions for all five blade designs. CB 75% shows  
336 the highest lift coefficient at 0.5 blade span location with a peak value of 0.182 while CB 100% shows  
337 the lowest lift coefficient value of 0.0835 amongst all the blades designed. Interestingly, Figures 11  
338 and 12 illustrate that the pressure is higher on the outer radius of trailing edge of the CB 100% (target  
339 shape blade), as compared to the other four blade geometries. This may be because the target shape  
340 is modelled as an assumption of the fish caudal fin and generates flow reattachment. Pressure near  
341 the tip region of all five designs increases as compared to the rest of the blade and the leading edge  
342 contributes to the pressure distribution increase on the pressure side. Simultaneously, the trailing edge  
343 causes negative pressure distribution increase on the suction side which contributes to lift force  
344 decrement and torque force reduction.

345

346 <Insert Figure 12 about here>

347

348 Figure 12 illustrates that variations in the pressure distribution yield the varying lift coefficient  
349 distribution on the airfoil chord length. The lift coefficient increases with the increase in blade span  
350 until 0.8 blade span location, after which a drastic reduction near the blade tip occurs. Although the  
351 lift coefficient varies in magnitude for all the blade designs, it can be observed that the CB 100%  
352 results in lower lift coefficients when compared to the other four blade designs. Therefore, it can be  
353 concluded from the steady state analysis that the target shape blade (i.e. CB 100%) would cause drag  
354 increase. This would cause torque reduction, leading to a lower power coefficient as the bend on the  
355 blade increases.

356

### 357 **Transient CFD analysis**



358 Transient simulations for the five blade designs were generated using the LES-Smagorinsky sub-grid  
359 scale model and fine unstructured mesh in an integrated time step. For all five design LES cases, the  
360 time step used for the simulation required for the flow to pass entirely through the turbine was about  
361 0.15million time steps. The time step size for each case was set to  $3 \times 10^{-5}$  which coincides with  
362 approximately ten blade rotations for the TSR = five for all five cases, which is equivalent to  $4.89 \times$   
363  $10^5$  seconds or 135.83 hours. Multiple frames of reference (MFR) was applied to the turbine disc  
364 analysis as it was a rotating domain based on the general grid interface (GGI) available in CFX. The  
365 turbulence intensity at the inlet of the computational domain was defined as 15% (typical seawater  
366 value) and as the tidal turbine blade geometry is a high turbulence intensity case. It should be noted  
367 that the non-uniform velocity of 2.5 m/s was applied to all five blade designs. The turbulence intensity  
368 gradually decreased at a distance of four rotor diameters downstream from the inlet to 13.68% due to  
369 velocity instability, and the turbulence level at the rotor leading edge was observed to be 12.82%.  
370 This gradual decrease was expected due to the higher rotational velocity of the blades which  
371 correspond to the blade tip. At the solid boundaries (blade geometry) the near wall node was  $y^+ = 50$   
372  $< y^+ < 300$  (Piomelli and Balaras, 2002; Tessicini and Leschziner, 2007) because of the two zonal  
373 layer LES approach used and the refined fine mesh in the tidal turbine domain was embedded into  
374 the ocean flow domain. The mesh parameter values for LES- Smagorinsky simulations are  
375 reproduced in Table 6.

376

377

378

<Insert Table 6 about here>

379

380

381

The residuals convergence criterion for each time step was set to  $10^{-5}$  and two monitors were used  
namely (Oberkampf *et al.*, 2004; Lim *et al.*, 2012; Versteeg and Malalasekera, 2007):

382

383

384

385

386

387

388

389

- Scaled residual monitors for mass and momentum of the iterative process; and
  - Lift coefficient  $C_L$  trend as a function of the iteration number for LES-Smagorinsky solution.
- The CFD solution is considered to have converged when the mass and momentum residuals present  
a constant trend under  $10^{-5}$  value which is illustrated in Figure 13 where the residuals represent the  
downward trend of the scaled residuals for the CB 75% LES-Smagorinsky solution.

390

391

392

393

394

395

396

397

398

399

400

401

402

403

404

<Insert Figure 13 about here>

Figure 13 illustrates that the residuals mark the continual removal of the unwanted imbalances thereby  
causing the CFD iterative process to converge rather than diverge. The mass residual at the time step  
number 1795 reached the convergence value of  $7.269e^{-06}$  and  $9.51e^{-06}$  on the time step 2665 when the  
transient solution was stopped. The discretised mass and momentum equations are presumed to be  
converged when they reached the convergence criterion and did not change with further iterations.  
The mass flow balance between the inlet and outlet were also verified for all the transient CFD  
simulations performed to ensure continuity of the solution (CFX-Solver Theory Guide, 2009;  
Oberkampf and Trucano, 2000). The lift coefficient ( $C_L$ ) history over iterations was also monitored  
to check the unsteady convergence of the LES-Smagorinsky solution (refer to Figure 14 for CB 75%).  
There was no appreciable change observed in the lift coefficient after 1100 timesteps but the solution  
was still monitored for more than 1500 time steps as the lift coefficient elevations to the fixed value  
of 0.1795.

405

406

407

408

409

<Insert Figure 14 about here>

LES transient simulations conducted sought to compare the results obtained with the steady state SST  
simulations. The turbine pressure contours (LES-Smagorinsky) (Figure 15) illustrate that a difference  
between the pressure and suction sides of the blade becomes smaller as the rotational velocity  
increases on the upper part of the blade. In comparison to steady state simulations, this increases the  
net lift and torque.

410  
411 <Insert Figure 15 about here>  
412

413 The pressure prediction on the tip of the blade (where the rotational velocity of the blade is at its  
414 highest) also causes higher lift on the pressure side of the blade. Figure 16 reveals that lift distribution  
415 on the suction side of the mid-height is larger than on the pressure side of the airfoil. This scenario  
416 significantly increases drag force on the CB 100% (target shape) as compared to the other four  
417 geometries, making it directly proportional to the bend on the blade. It also illustrates that the most  
418 affected region by the seawater is the tip chord of the blade along leading and trailing edges. The  
419 drag increment for the CB 100% was expected seeing the negative pressure on the suction side on the  
420 tip, proving to generate cavitation in extreme velocity conditions.  
421

422 <Insert Figure 16 about here>  
423

424 The LES simulations demonstrate that the kinetic energy contained in the seawater flow is extracted  
425 from the blade's upper stream and that pressure prediction is more realistic as there is no flow  
426 divergence in real life HATT's. The prediction of the lift caused due to the large separation of the  
427 flow and the pressure surface of the blades consequently increases the predicted power coefficients,  
428 and causes less discrepancy in the vorticity of the pressure field. Interestingly, LES solutions with a  
429 high computational overhead demonstrate a clear phenomenon of the pressure changes on the blade  
430 and avoids over prediction of the lift and power coefficient.  
431

#### 432 **DISCUSSION OF THE COMPARISON BETWEEN THE DESIGNED BLADES**

433 The performance of SST and LES-Smagorinsky turbulence models are examined by plotting the lift  
434 coefficient against various angles of attack (refer to Figure 17). There is a gradual decrease in the lift  
435 coefficient after the six degrees of angle of attack for all the cases, as the flow becomes highly non-  
436 linear and the rotational velocity of the blades reaches its maximum. The mass flow rate of the  
437 seawater is a function of the cross-sectional area of the turbine blades and its velocity, therefore the  
438 bend on the curved blades makes the mass flow rate drop the lift coefficient after 6 degrees of angle  
439 of attack.  
440

441 <Insert Figure 17 about here>  
442

442 Therefore, it can be concluded that with the increase in the angle of attack the turbine blades would  
443 rotate faster but simultaneously kinetic energy available in the seawater exerts a drag force upon the  
444 blade, causing a reduction of the overall power coefficient of the turbine blade. The output power  
445 notably depends on the inlet seawater velocity (refer to Figure 18). Although the CB 100% yields  
446 almost 15% more power than the SB in case of all the flow velocities, this does not necessarily mean  
447 that it would yield the highest power coefficient for the designed blades.  
448

449 <Insert Figure 18 about here>  
450

451 The SB produces 366 kW of power and a power coefficient of 0.4028, whilst the CB 100% provides  
452 approximately 20% more output power than the SB, and about 15% more power than the most  
453 efficient CB 75%. However, the power coefficient for the target shape blade i.e. CB 100% is 0.3951  
454 and 0.3728 for the SST and LES-Smagorinsky CFD simulations respectively. As 80% of turbine  
455 blade efficiency (i.e. the power coefficient) is generated from the midsection of the designed blade to  
456 the tip of the blade. The CB 75% showed the most consistent and efficient set of data from the SST  
457 and the LES-Smagorinsky CFD tests. There was little difference between the results from the LES-  
458 Smagorinsky CFD simulations but these results confirm the accuracy of the comparative analysis  
459 while using two different turbulence modelling techniques. Therefore, the CB 75% will be put  
460 forward to allow the coefficient power comparison with the standard (suitable) HATT models  
461 available in the tidal turbine literature.

462 Goundar and Ahmed (2013) designed a three bladed 10m diameter HATT, and achieved a maximum  
463 efficiency of 47.5% with a power output of 150kW, for the constant seawater velocity of 2m/s. The  
464 CB 75% is also three bladed and has a 14.2 diameter, and yields an efficiency of 51.78% for LES  
465 simulations with a power output of 435kW; which is higher than the overall efficiency achieved by  
466 Goundar and Ahmed [9]. At the same time the benefit of designing a blade like a CB generates higher  
467 lift and power coefficients at lower and higher tidal current velocities, and this has been demonstrated  
468 with the CFD simulations presented above. The STAR blade to generate low-cost electricity from  
469 wind designed by Larwood & Zuteck (2006) implements swept blade design parameters and produces  
470 annual power output which ranges from 1.5 to 3MW. The designed turbine blades are 71 to 126m in  
471 diameter and have rated generator speed of 1800rpm, and the designed swept wind turbines produce  
472 10 to 15% more power than the standard wind turbines available in the current market. A direct  
473 comparison between the results obtained from this research with the STAR blade is beyond the scope  
474 of this research, as the maximum diameter a tidal turbine can have 22m (Bahaj *et al.*, 2007; Bahaj *et*  
475 *al.*, 2007; Batten *et al.*, 2008), and as the designed CB 75% is 14.4m in diameter. A general  
476 comparison of the annual power output can be made, i.e. designing the curved caudal fin blades  
477 produces at least 10% more annual power output than the standard straight blades which has been  
478 shown by both the studies i.e. by this research and by Larwood & Zuteck (2006).

479 In summary, analysis results confirms that bio-mimicking the caudal fin look-alike turbine blade i.e.  
480 CB 75%, produces greater efficiency than the default SB which was designed according to the tidal  
481 turbine blade literature and meets the aim of this paper.

## 483 CONCLUSIONS

484 It can be concluded that although LES-Smagorinsky provides a better result than the SST simulations,  
485 it also has a massive computational overhead. The CFD results allow a further comparison of the  
486 power coefficients; proving that a CB produces more efficiency than the standard HATT's at lower  
487 and higher tidal current velocities. The most fundamental challenge confronting this research was to  
488 validate the CFD methodology for the case studies performed with real world data. This is also the  
489 most significant problem faced in the wind turbine industry, to which this research could contribute.  
490 To overcome this challenge, a comparative analysis was performed for the SB and CB 75% with the  
491 tidal turbine literature which thus helps the future tidal turbine blade designers in knowledge transfer,  
492 particularly on turbulence model selection. A mesh independency study of a straight blade to  
493 determine the mesh sensitivity and its effects on the CFD simulation results. The grid convergence  
494 study was simulated using two turbulence models: the standard k- $\epsilon$  model, and SST turbulence model  
495 at coarse, medium, and fine mesh resolution thus simulating six different mesh sizes. This paper has  
496 shown that obtaining mesh independent solutions is a fundamental need for all the tidal turbine blade  
497 designers due to the sensitivity of the lift coefficient of the tidal turbine.

498  
499 The standard k- $\epsilon$  model under predicts the power coefficients and the simulation time is highly  
500 dependent on the mesh and turbulence model chose for CFD analysis. The highest CP obtained from  
501 the mesh independent study conducted is 0.4218 for M3 from SST model and the lowest CP 0.2693  
502 for M6 using k- $\epsilon$  model. M2 and M3 account for nearly 1% difference in the estimated power  
503 coefficients, but the final CFD simulation time required for convergence of the two meshes is  
504 substantially different when conventional mesh independency method is employed. Pressure  
505 distribution is a predominant output for determining the lift, and power coefficients, and also to define  
506 the most efficient blade. Lift coefficient distribution across blade spans showed a similar trend of the  
507 peak lift coefficient being observed at 0.75 to 0.8 of the total blade span before drastically dropping  
508 down at 0.9 onwards due to the increasing rotational velocity of the blades.

509  
510 The unsteady convergence is an iterative process of the transient solution which needs to be monitored  
511 to calculate the accuracy of the transient CFD solution. This was done by monitoring the scaled  
512 residuals for mass, and momentum and observing lift coefficient as a function of the iteration. The  
513 removal of unwanted imbalances over time steps result in the CFD solution to converge and do not

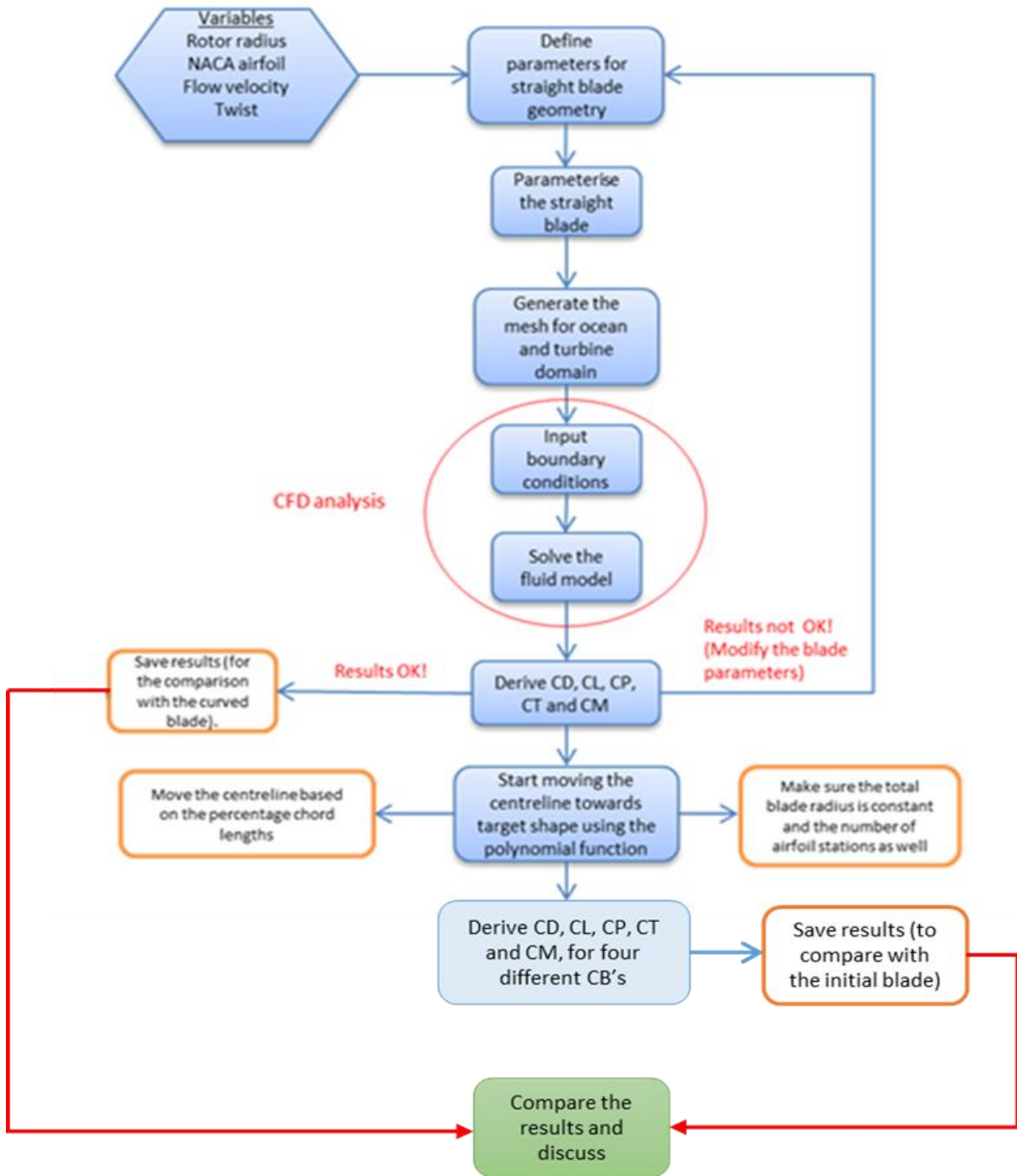
514 change with further iterations. Future work derived from the observations made from this research  
515 should seek to develop a design automation closed loop system using Knowledge Based Engineering  
516 (KBE) principles to design a robust tidal turbine blade design which would be optimal throughout the  
517 year. The designed closed loop system would automatically parameterize blade geometry, generate  
518 automatic mesh, and the numerical results by itself.  
519

520 **REFERENCES**

- 521 Afgan I, McNaughton J, Rolfo S, Apsley DD, Stallard T, Stansby P. (2013) Turbulent flow and  
522 loading on a tidal stream turbine by LES and RANS. *International Journal of Heat and Fluid*  
523 *Flow*. Vol. 43, pp. 96–108.
- 524 ANSYS INC. CFX-Solver Theory Guide 2009.
- 525 Bahaj AS, Batten WMJ, McCann G. (2007) Experimental verifications of numerical predictions for  
526 the hydrodynamic performance of horizontal axis marine current turbines. *Renewable Energy*.  
527 Vol. 32, pp. 2479–90.
- 528 Bahaj AS, Molland AF, Chaplin JR, Batten WMJ. (2007) Power and thrust measurements of marine  
529 current turbines under various hydrodynamic flow conditions in a cavitation tunnel and a towing  
530 tank. *Renewable Energy*. Vol.32, pp. 407–26.
- 531 Bai G, Li W, Chang H, Li G. (2016) The effect of tidal current directions on the optimal design and  
532 hydrodynamic performance of a three-turbine system. *Renewable Energy*. Vol. 94, pp. 48–54.
- 533 Batten WMJ, Bahaj AS, Molland AF, Chaplin JR. (2008) The prediction of the hydrodynamic  
534 performance of marine current turbines. *Renewable Energy*. Vol. 33, pp. 1085–96.
- 535 Bin JI, LUO X, PENG X, WU Y. (2013) Three-dimensional large eddy simulation and vorticity  
536 analysis of unsteady cavitating flow around a twisted hydrofoil. *Journal of Hydrodynamics*.  
537 Vol.25, pp. 510–9.
- 538 Blackmore T, Myers LE, Bahaj AS. (2016) Effects of turbulence on tidal turbines: Implications to  
539 performance, blade loads, and condition monitoring. *International Journal of Marine Energy*.  
540 Vol. 14, pp. 1–26.
- 541 Boris JP, Grinstein FF, Oran ES, Kolbe RL. (1992) New insights into large eddy simulation. *Fluid*  
542 *Dynamics Research*. Vol. 10, pp. 199–228.
- 543 Campi MC, Lecchini A, Savaresi SM. (2002) Virtual reference feedback tuning: a direct method  
544 for the design of feedback controllers. *Automatica*. Vol.38, pp. 1337–46.
- 545 Churchfield MJ, Li Y, Moriarty PJ. (2013) A large-eddy simulation study of wake propagation and  
546 power production in an array of tidal-current turbines. *Philos Trans R Soc London A Math Phys*  
547 *Eng Sci*. Vol. 371:20120421
- 548 Ciri U, Rotea M, Santoni C, Leonardi S. (2016) Large Eddy Simulation for an array of turbines with  
549 Extremum Seeking Control. American Control Conference, Boston, MA, USA, pp. 531–6.
- 550 Divett T, Vennell R, Stevens C. (2013) Optimization of multiple turbine arrays in a channel with  
551 tidally reversing flow by numerical modelling with adaptive mesh. *Phil Trans R Soc A*. Vol.  
552 371, 20120251.
- 553 Divett T, Vennell R, Stevens C. (2016) Channel-scale optimisation and tuning of large tidal turbine  
554 arrays using LES with adaptive mesh. *Renewable Energy*. Vol. 86, pp. 1394–405
- 555 Funke SW, Farrell PE, Piggott MD. (2014) Tidal turbine array optimisation using the adjoint  
556 approach. *Renewable Energy*. Vol. 63, pp. 658–73.
- 557 Gayen B, Sarkar S. (2011) Direct and large-eddy simulations of internal tide generation at a near-  
558 critical slope. *Journal of Fluid Mechanics*. Vol. 681 pp. 48–79.
- 559 Goundar JN, Ahmed MR. (2013) Design of a horizontal axis tidal current turbine. *Applied Energy*.  
560 Vol. 111, pp. 161–74.
- 561 Harrison ME, Batten WMJ, Myers LE, Bahaj AS. (2010) Comparison between CFD simulations  
562 and experiments for predicting the far wake of horizontal axis tidal turbines. *IET Renewable*  
563 *Power Generation*. Vol. 4, pp. 613–27.
- 564 Hudgins DW, Lavelle JP. (1995) Risk management in design engineering bids. University of North  
565 Texas Libraries, Digital Library, Kansas City, Missouri.
- 566 Jo C-H, Lee J-H, Rho Y-H, Lee K-H. (2014) Performance analysis of a HAT tidal current turbine  
567 and wake flow characteristics. *Renewable Energy*. Vol. 65, pp. 175–82
- 568 Kang S, Borazjani I, Colby JA, Sotiropoulos F. (2012) Numerical simulation of 3D flow past a real-  
569 life marine hydrokinetic turbine. *Advances in Water Resources*. Vol. 39, pp. 33–43.
- 570 Kim K-P, Ahmed MR, Lee Y-H. (2012) Efficiency improvement of a tidal current turbine utilizing  
571 a larger area of channel. *Renewable Energy*. Vol. 48, pp. 557–64.

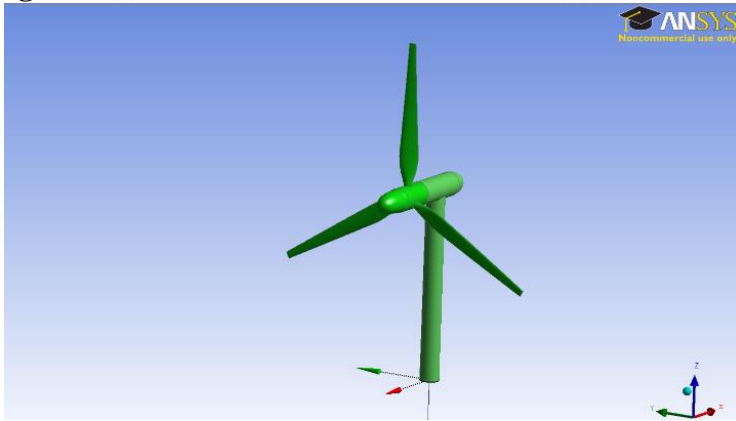
- 572 Larwood S, Zuteck M. (2006) Swept wind turbine blade aeroelastic modeling for loads and dynamic  
573 behavior. *AWEA Wind*. pp. 1–17.
- 574 Li C, Zhu S, Xu Y, Xiao Y. (2013) 2.5 D large eddy simulation of vertical axis wind turbine in  
575 consideration of high angle of attack flow. *Renewable Energy*. Vol. 51, pp. 317–30.
- 576 Li M, Radhakrishnan S, Piomelli U, Rockwell Geyer W. (2010) Large-eddy simulation of the tidal-  
577 cycle variations of an estuarine boundary layer. *Journal of Geophysical Research Ocean*. Vol.  
578 115.
- 579 Liu P. (2010) A computational hydrodynamics method for horizontal axis turbine--Panel method  
580 modeling migration from propulsion to turbine energy. *Energy*. Vol. 35, pp. 2843–51.
- 581 Malki R, Masters I, Williams AJ, Croft TN. (2014) Planning tidal stream turbine array layouts using  
582 a coupled blade element momentum--computational fluid dynamics model. *Renewable Energy*.  
583 Vol. 63, pp. 46–54.
- 584 McSherry R, Grimwade J, Jones I, Mathias S, Wells A, Mateus A. (2011) 3D CFD modelling of  
585 tidal turbine performance with validation against laboratory experiments. 9th European Wave  
586 Tidal Energy Conference, University of Southampton, UK.
- 587 Mo J-O, Choudhry A, Arjomandi M, Lee Y-H. Large eddy simulation of the wind turbine wake  
588 characteristics in the numerical wind tunnel model. *Journal of Wind Engineering and Industrial  
589 Aerodynamics*. Vol. 112, pp. 11–24.
- 590 Oberkampf WL, Trucano TG, Hirsch C. (2004) Verification, validation, and predictive capability in  
591 computational engineering and physics. *Applied Mechanics Reviews*. Vol. 57, pp. 345–84.
- 592 Oberkampf WL, Trucano TG. (2000) Validation methodology in computational fluid dynamics.  
593 Fluids 2000 Conference and Exhibit Denver, CO, U.S.A. pp. 19–22.
- 594 Piomelli U, Balaras E. (2002) Wall-layer models for large-eddy simulations. *Annual Reviews in  
595 Fluid Mechanics*. Vol. 34, pp. 349–74.
- 596 Roc T, Conley DC, Greaves D. (2013) Methodology for tidal turbine representation in ocean  
597 circulation model. *Renewable Energy*. Vol. 51, pp. 448–64.
- 598 Rocha PAC, Rocha HHB, Carneiro FOM, da Silva MEV, Bueno AV. (2014) k- $\omega$  SST (shear stress  
599 transport) turbulence model calibration: A case study on a small scale horizontal axis wind  
600 turbine. *Energy*. Vol. 65. pp. 412–8.
- 601 Sescu A, Meneveau C. (2015) Large-Eddy Simulation and Single-Column Modeling of Thermally  
602 Stratified Wind Turbine Arrays for Fully Developed, Stationary Atmospheric Conditions.  
603 *Journal of Atmospheric and Oceanic Technology*. Vol. 32, pp. 1144–62.
- 604 Shen H, Li S, Chen G. (2012) Quantitative analysis of surface deflections in the automobile exterior  
605 panel based on a curvature-deviation method. *Journal of Materials Processing Technology*. Vol.  
606 212, pp. 1548–56.
- 607 Shi W, Wang D, Atlar M, Guo B, Seo K. (2015) Optimal design of a thin-wall diffuser for  
608 performance improvement of a tidal energy system for an AUV. *Ocean Engineering*. Vol. 108,  
609 pp. 1–9.
- 610 Tedds SC, Owen I, Poole RJ. (2014) Near-wake characteristics of a model horizontal axis tidal  
611 stream turbine. *Renewable Energy*. Vol. 63, pp. 222–35.
- 612 Tessicini F, Li N, Leschziner MA. (2007) Large-eddy simulation of three-dimensional flow around  
613 a hill-shaped obstruction with a zonal near-wall approximation. *International Journal of Heat  
614 and Fluid Flow*. Vol.28, pp. 894–908.
- 615 Thapar V, Agnihotri G, Sethi VK. (2011) Critical analysis of methods for mathematical modelling  
616 of wind turbines. *Renewable Energy*. Vol. 36, pp. 3166–77.
- 617 Versteeg HK, Malalasekera W. (2007) *An introduction to computational fluid dynamics: the finite  
618 volume method*. 2<sup>nd</sup> edition, Pearson Education, Essex, England.
- 619 Wang J, Piechna J, Mueller N. (2012) A novel design of composite water turbine using CFD.  
620 *Journal of Hydrodynamics*. Vol. 24, pp. 11–6.
- 621
- 622

623 **Figure 1** - Graphical Overview of the Direct Design Method Used

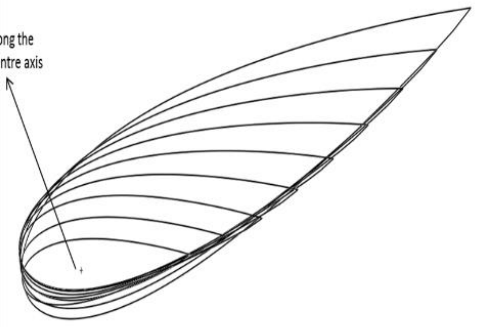


624  
625  
626

627 **Figure 1(a) - 3D Model of the SB HATT; 2(b) Non-linear Twist Distribution**



Twist along the blade centre axis



628  
629



630 **Table 1 - SB Parameters**

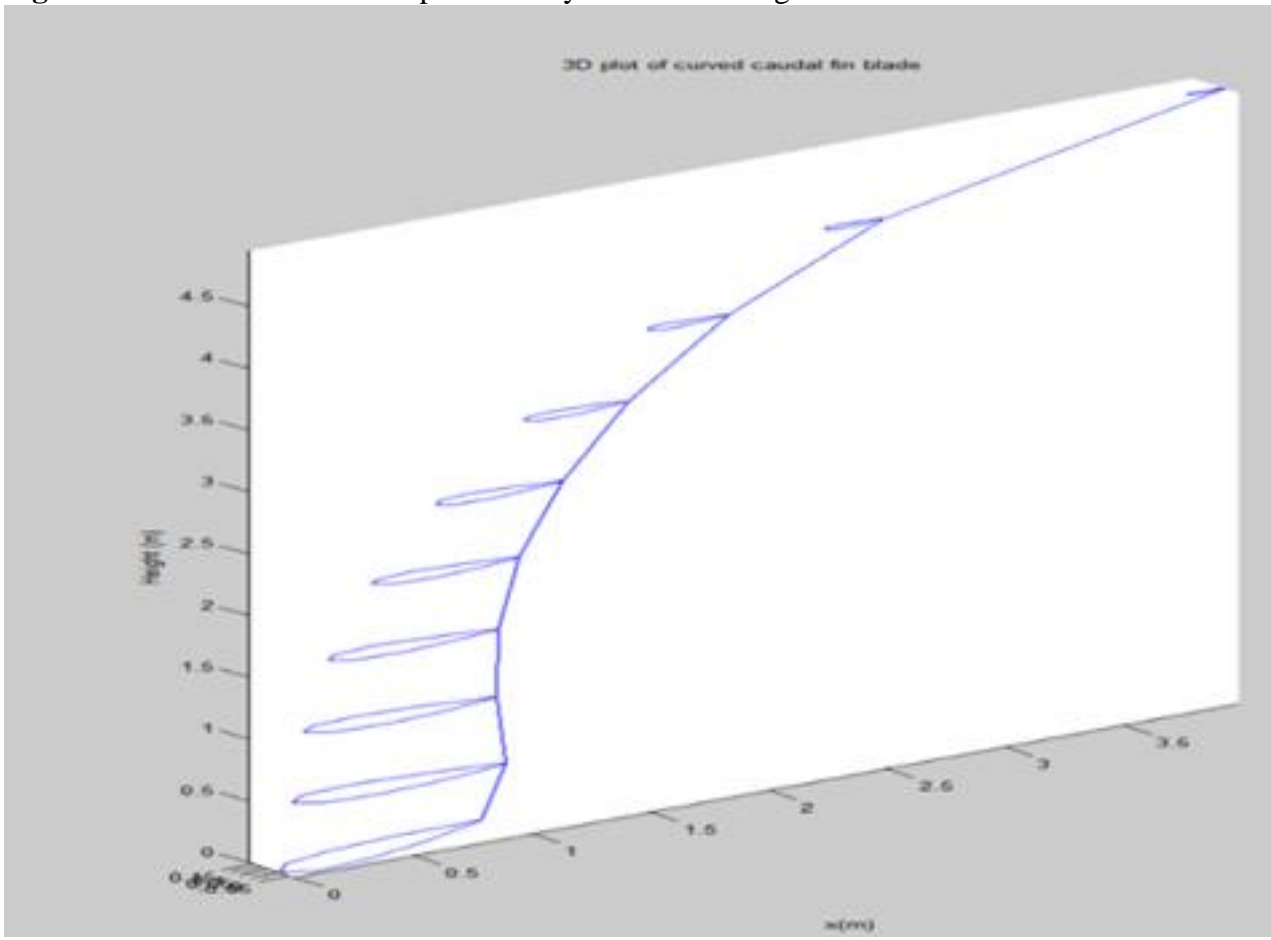
---

Number of blades	3
Radius	7.4 m
Airfoil	NACA 0018
Root airfoil chord length	1 m
Tip airfoil chord length	360 mm
Root airfoil twist	16°
Tip airfoil twist	4°

---

631  
632

633 **Figure 3** - 3D Plot of the CB Reproduced by MATLAB Program



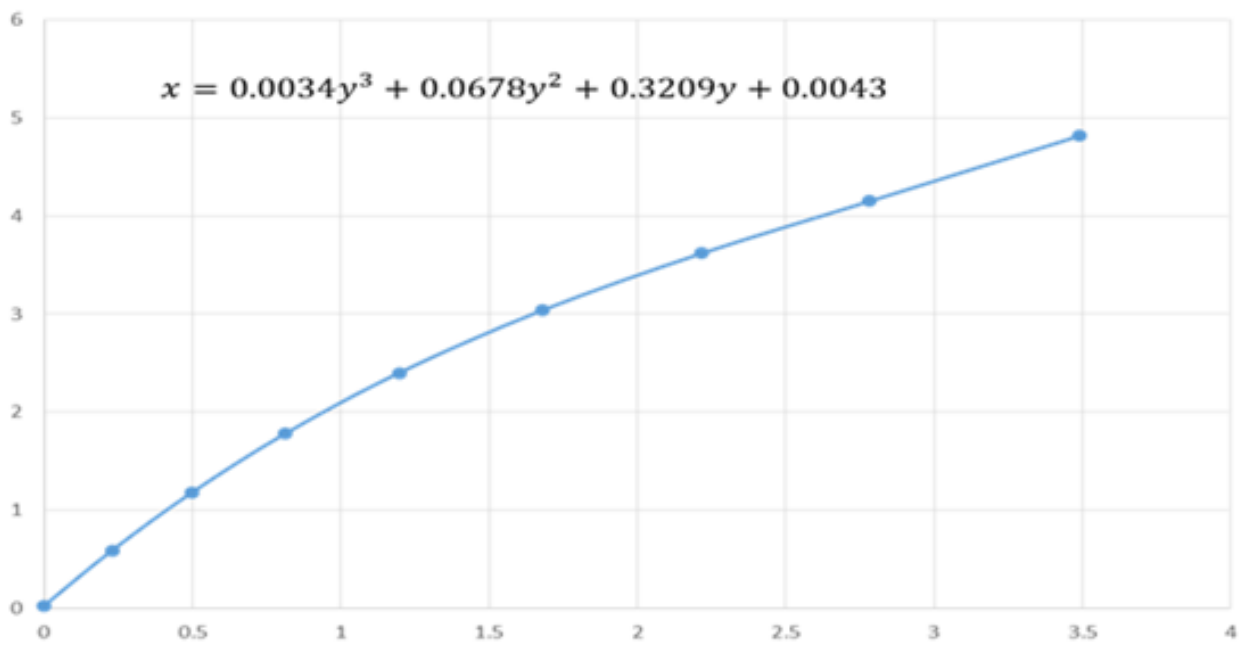
634  
635

636 **Table 2** - Default Values for Defining the Curved Blade Shape  
637

X- Offset	Y – Offset	Chord length, c (mm)
0	0	1645
0.2285	0.6	1337
0.4998	1.2	1091
0.8145	1.8	924
1.197	2.4	808
1.678	3	663
2.2164	3.6	509
2.7833	4.2	353
3.489	4.8	0

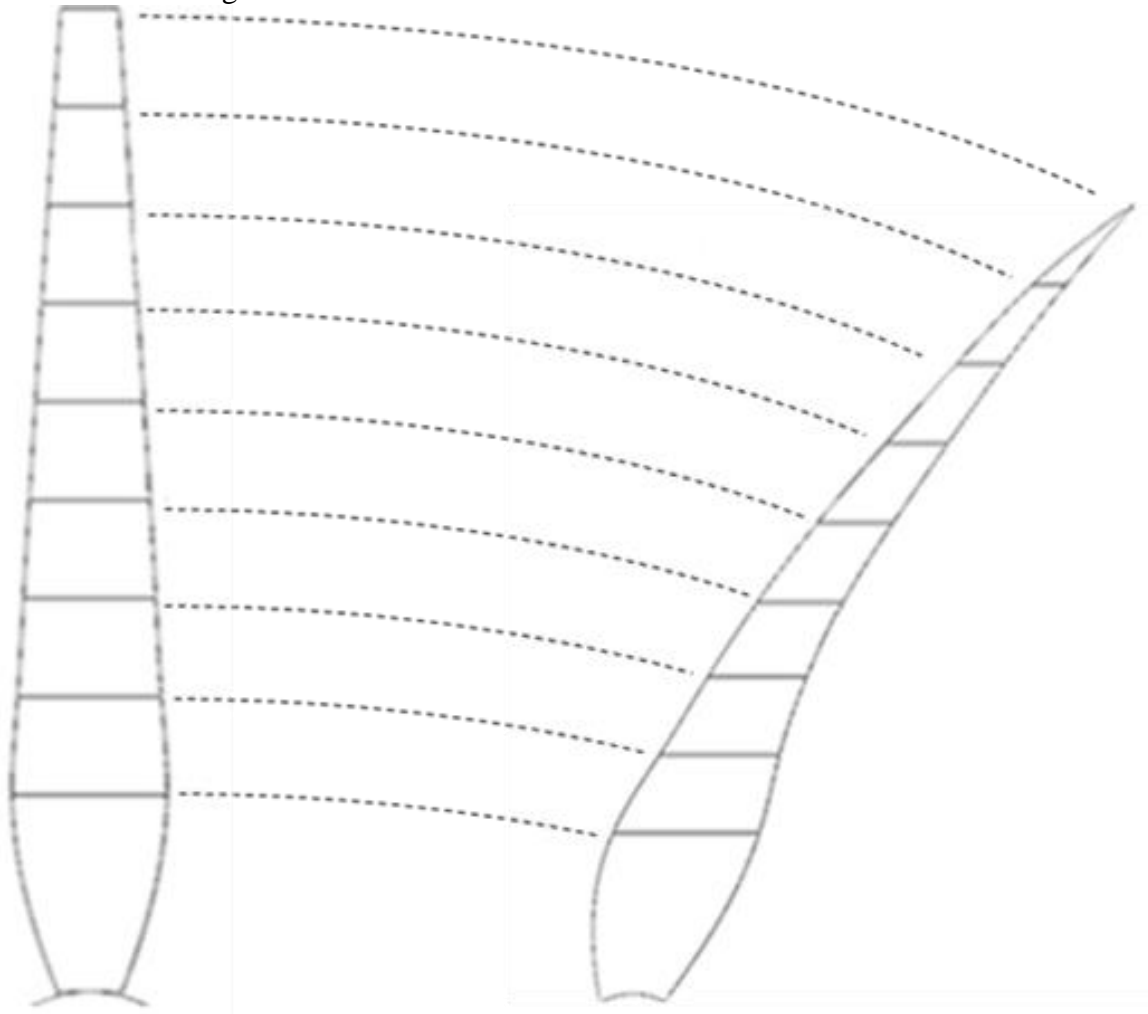
638  
639  
640

641 **Figure 4** - The Skeleton (Centre Line) of the CB Fitted with Third Order Polynomial Function



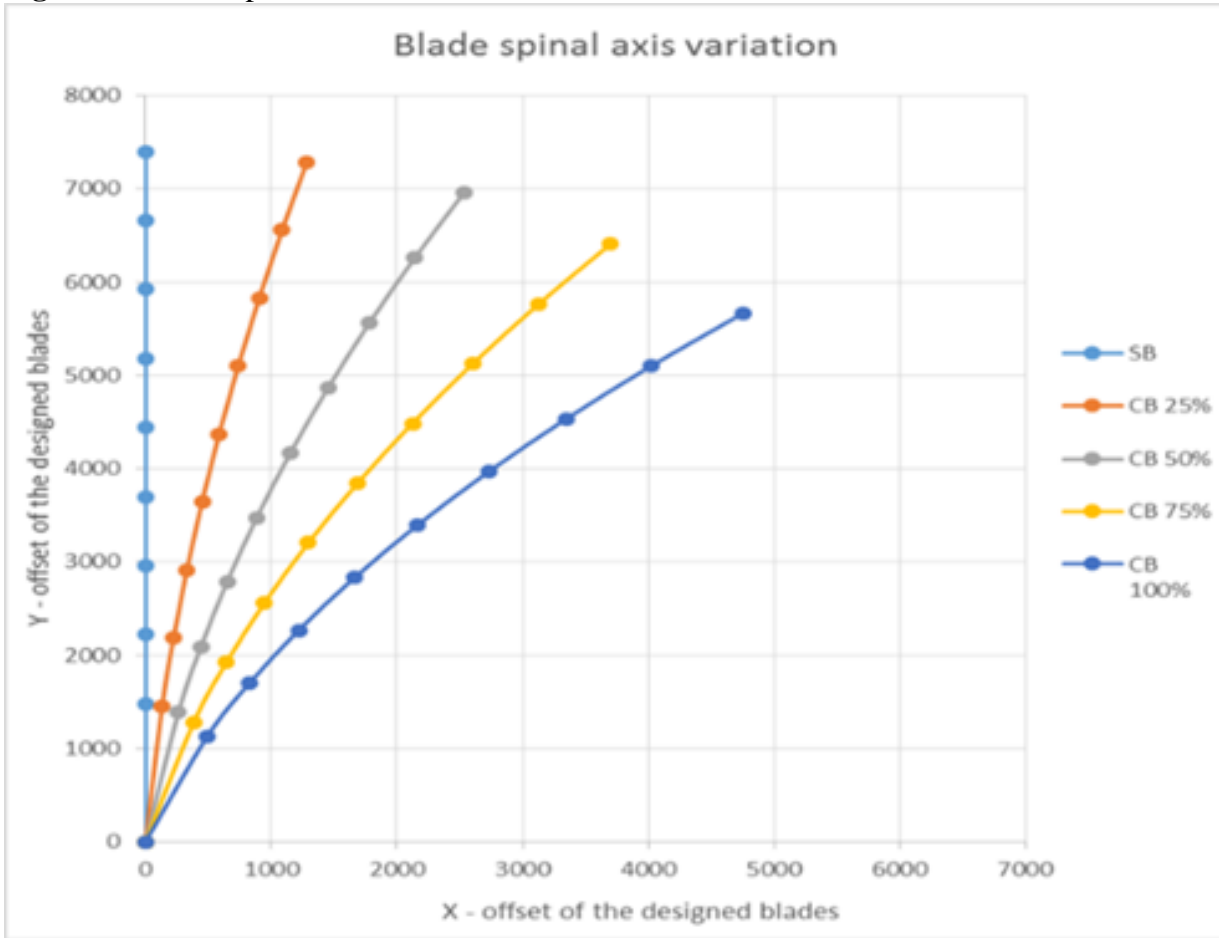
642  
643  
644  
645  
646

647 **Figure 5** - Chord Length Variation of the SB to Achieve CB



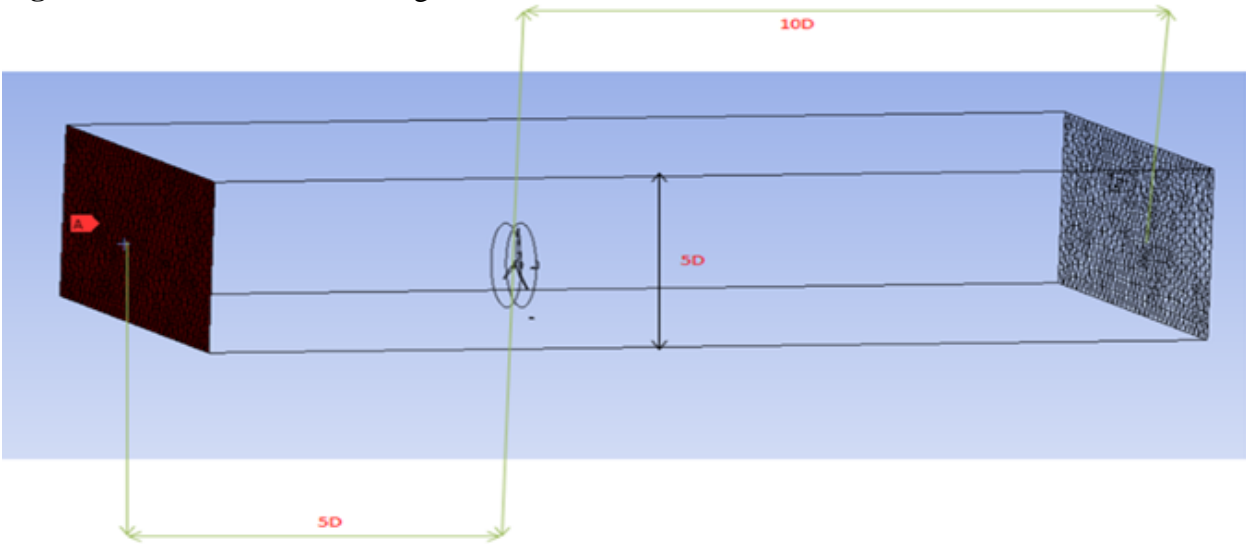
648  
649  
650

651 **Figure 6 - Blade Spinal Axis Variation**



652  
653

654 **Figure 7 - Inlet, Outlet, and Height Extension from the Turbine Blades**



655  
656  
657  
658

659

Table 3 Mesh size, CFD simulation time, and estimated  $C_P$  for SST model at  $\lambda = 5$ .

<b>Mesh Resolution</b>	Coarse (M1)	Mesh Medium (M2)	mesh	Fine mesh (M3)
<b>Number of nodes</b>	79859	151740		230439
<b>CFD simulation time</b>	4hrs 10mins	6hrs 16mins		9hrs 53mins
<b>Estimated <math>C_P</math></b>	0.3816	0.4169		0.4218

660

661

662

663

664

665

666

667

668

669

670

671

672

673

674

675

676

677

678

679

680

681



682

683

*Table 4 Mesh size, CFD simulation time, and estimated  $C_P$  for  $k-\varepsilon$  model at  $\lambda = 5$ .*

<b>Mesh Resolution</b>	Coarse mesh (M4)	Medium mesh (M5)	Fine mesh (M6)
<b>Number of nodes</b>	44064	92767	139506
<b>CFD simulation time</b>	1hr 36mins	4hrs 41mins	5hrs 38mins
<b>Estimated <math>C_P</math></b>	0.2271	0.2586	0.2693

684

685

686

687

688

689

690

691

692

693

694

695

696

697

698

699

700

701

702

703

704

705

706

707

708

709

710

711

712

713

714

715

716

717

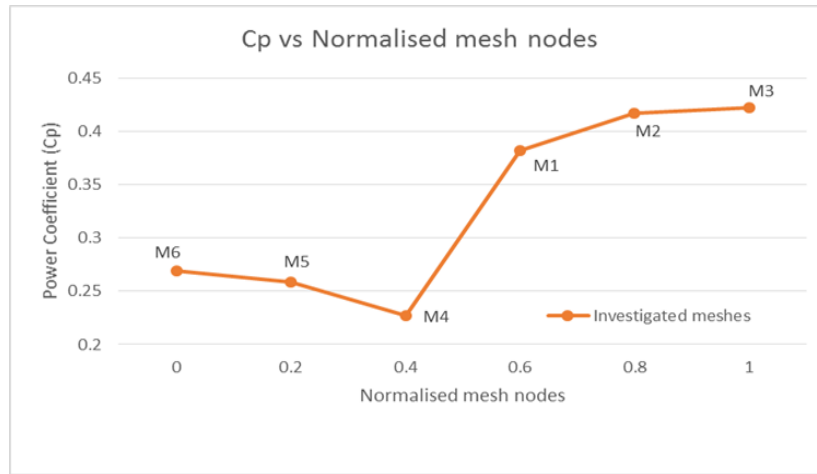
718

719

720

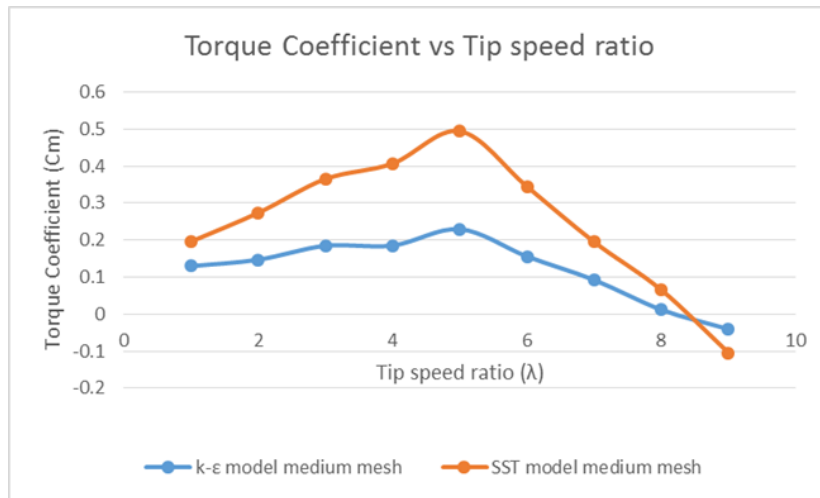
721  
722  
723  
724  
725  
726  
727  
728  
729  
730  
731  
732  
733  
734  
735  
736  
737  
738  
739  
740  
741  
742  
743  
744  
745  
746  
747  
748  
749  
750  
751  
752  
753  
754  
755  
756  
757  
758  
759  
760  
761  
762  
763  
764  
765  
766  
767  
768  
769

Figure 8 The power coefficients of all the investigated meshes in mesh independency study



770  
771  
772  
773  
774

**Figure 9 Torque coefficient versus Tip speed ratio for  $k-\epsilon$  and SST model medium meshes**

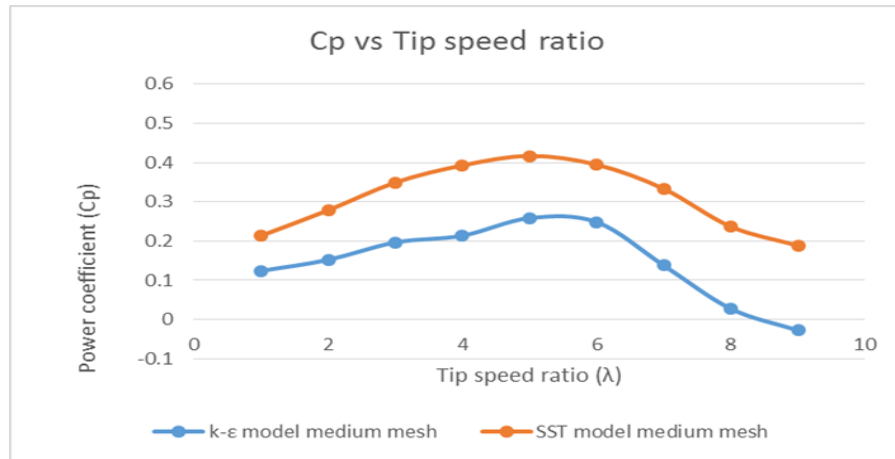


775  
776  
777  
778  
779  
780  
781  
782  
783  
784  
785  
786  
787  
788  
789  
790  
791  
792  
793  
794  
795  
796  
797  
798  
799  
800  
801  
802  
803  
804  
805

806  
807

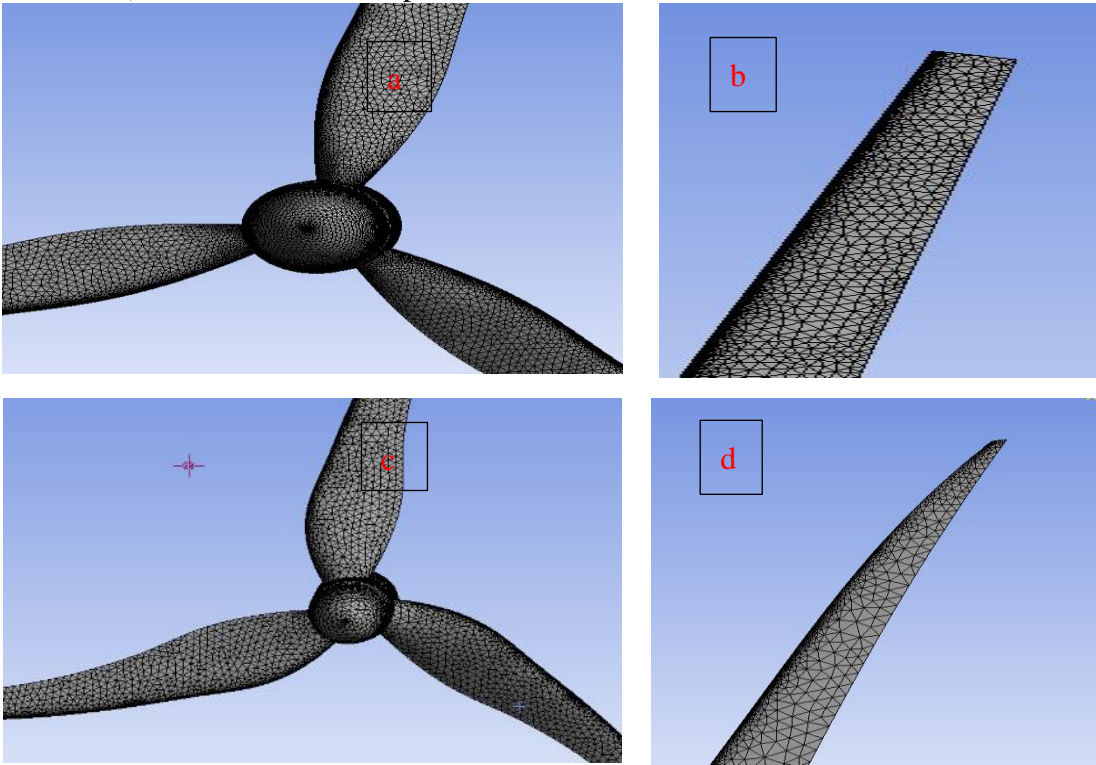
808 *Figure 10 Power coefficient versus tip speed ratio for k-ε and SST model medium meshes*

809  
810  
811  
812  
813  
814  
815  
816  
817  
818  
819  
820  
821  
822  
823  
824  
825  
826  
827  
828  
829  
830  
831  
832  
833  
834  
835  
836  
837  
838  
839  
840  
841  
842  
843  
844  
845  
846  
847  
848  
849  
850  
851  
852  
853  
854  
855



856  
857  
858  
859

**Figure 11** - a) Meshed SB with Blades and Hub, b) SB Meshed Tip, c) Meshed 75% CB with Blades and Hub, d) 75% CB Meshed Tip



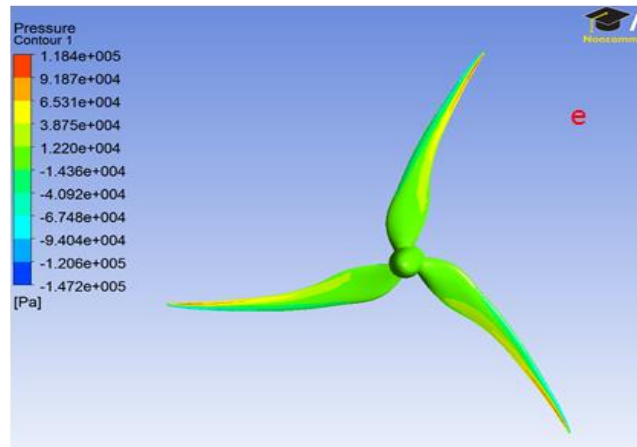
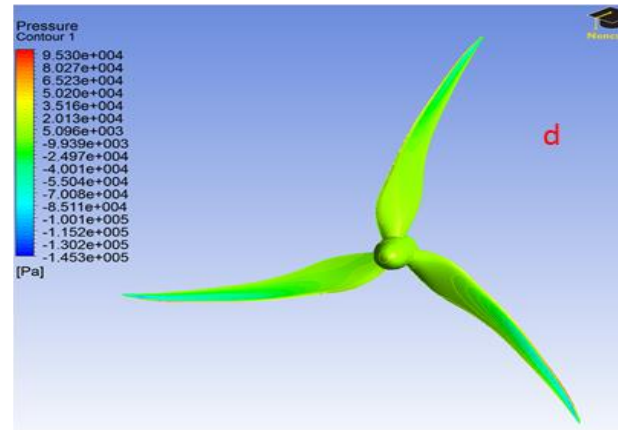
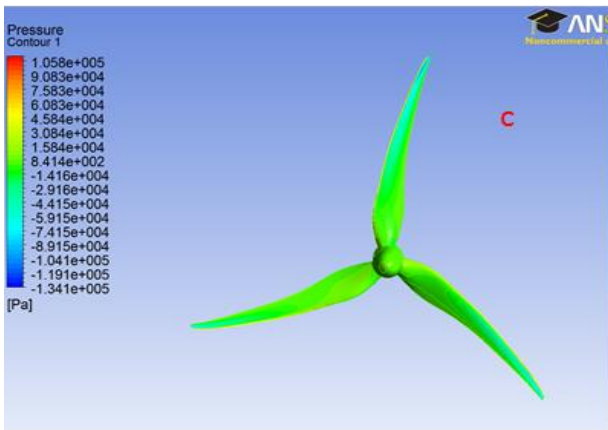
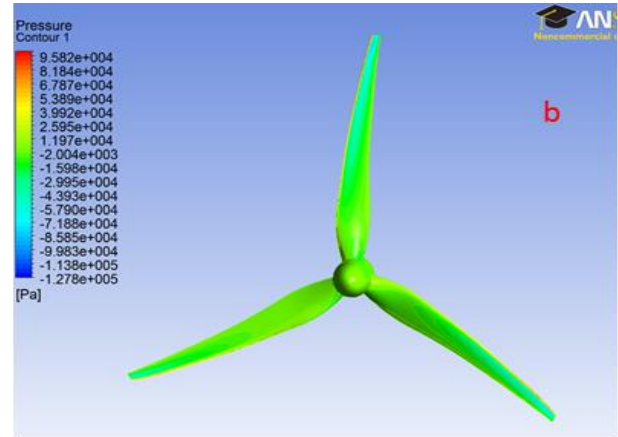
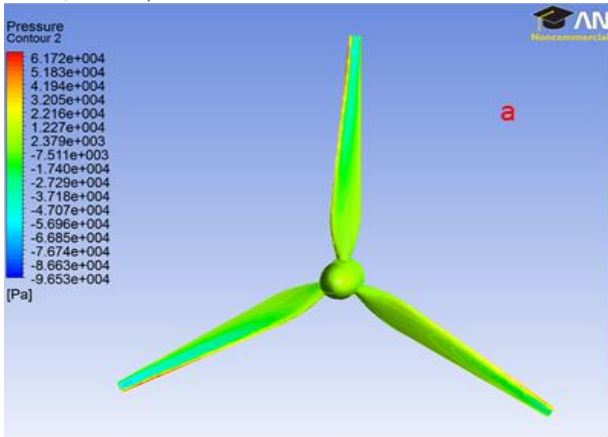
860  
861

862 **Table 5** - Mesh Parameters for all the Designed Blades (SST)

Blade Model	Mesh growth rate	Maximum mesh size (mm)	Minimum mesh size (mm)	Curvature normal angle (°)	Number of nodes
SB	1.2	2500	75	15	151740
CB 25%	1.15	2100	50	13	195647
CB 50%	1.10	1800	45	11	226846
CB 75%	1.05	1500	40	10	252839
CB 100%	1.0	1150	35	10	309461

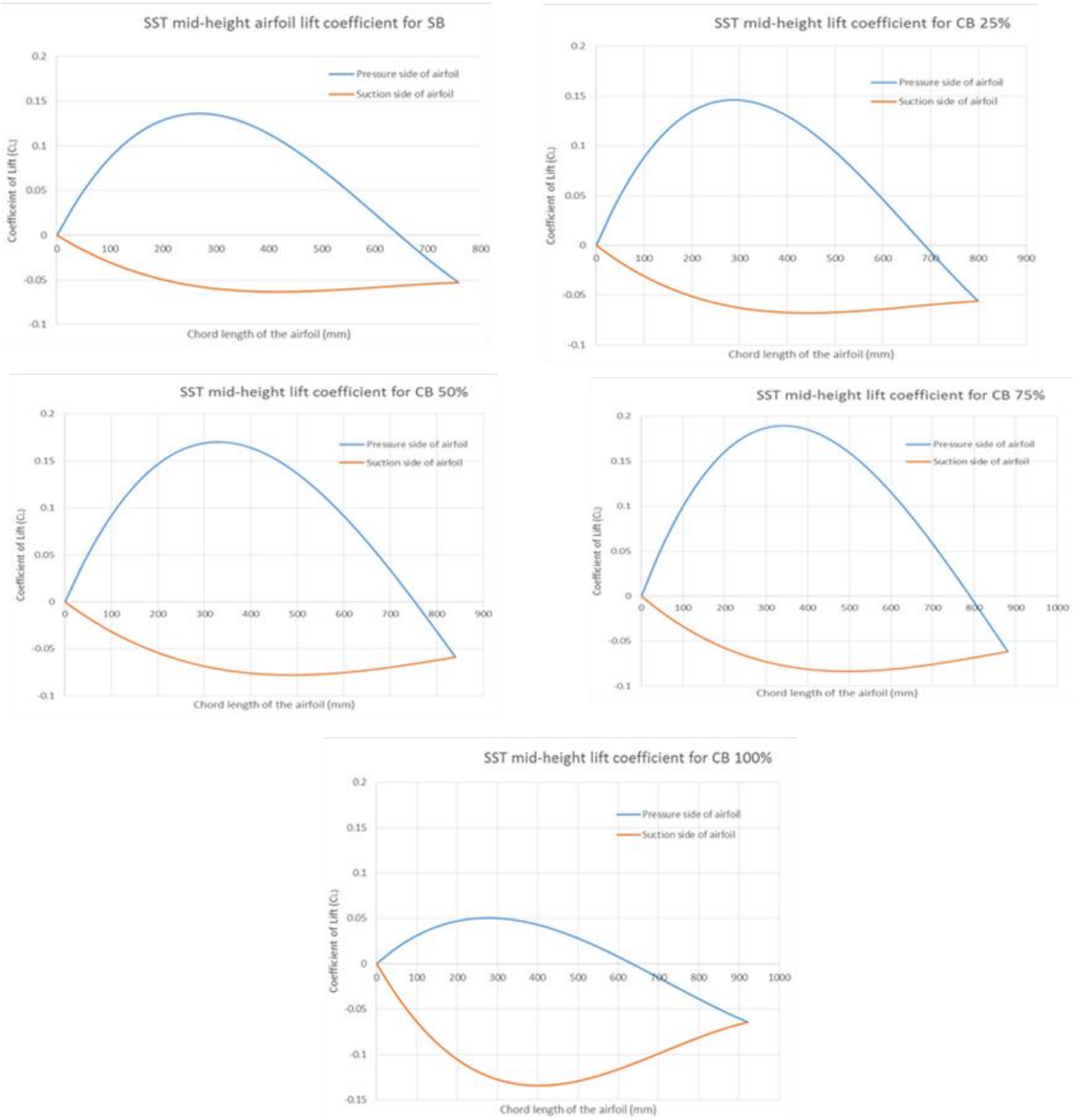
863  
864  
865

866 **Figure 12** - Blade Pressure Distributions (Pressure Side) on a) SB, b) CB 25 %, c) CB 50%, d) CB  
867 75%, and e) CB 100%



868  
869  
870

871 **Figure 13 - SST Mid-height Lift Coefficient Distribution for Five Blade Designs**  
 872



873  
 874  
 875



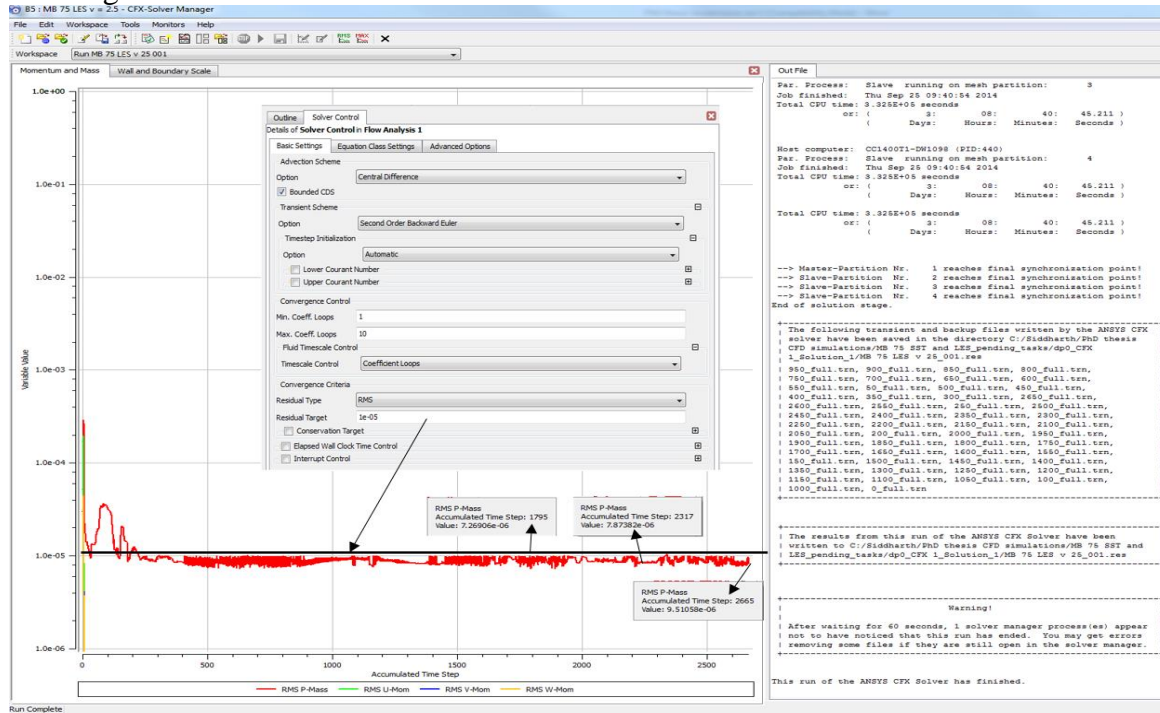
876 **Table 6 - Mesh Parameters for the Designed Blades (LES-Smagorinsky)**

Blade Model	Mesh growth rate	Maximum mesh size (mm)	Minimum mesh size (mm)	Curvature normal angle (°)	Number of nodes
SB	1.0	1150	65	10	427552
CB 25%	0.85	950	45	9	514842
CB 50%	0.7	820	40	7	690137
CB 75%	0.55	760	38	6	851326
CB 100%	0.4	680	35	6	912470

877  
878

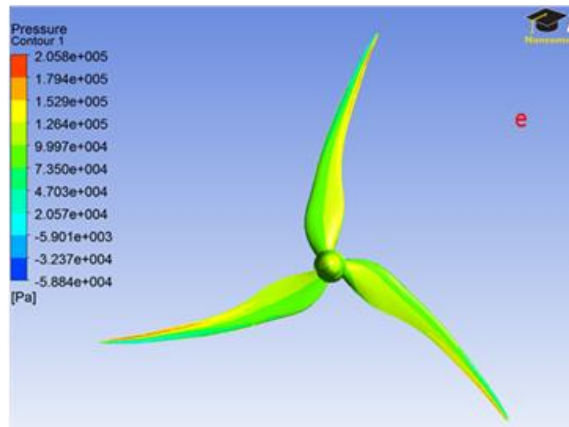
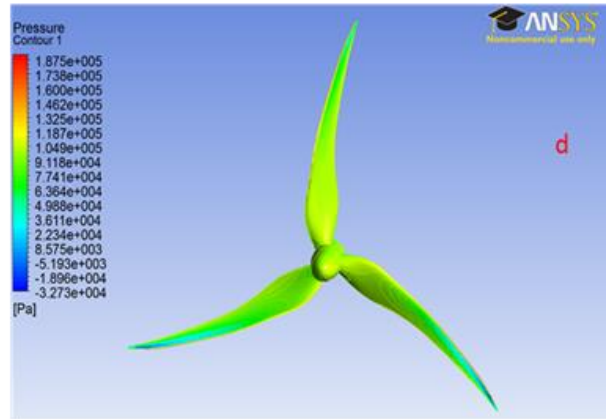
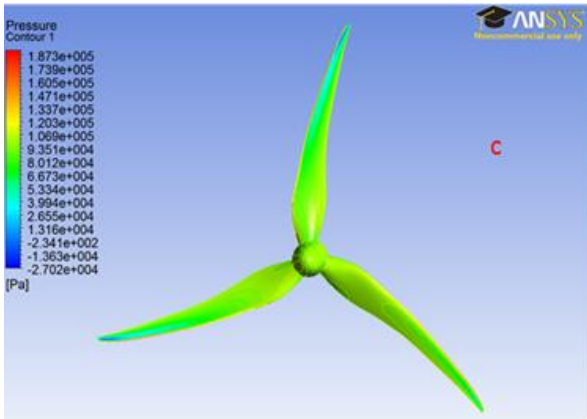
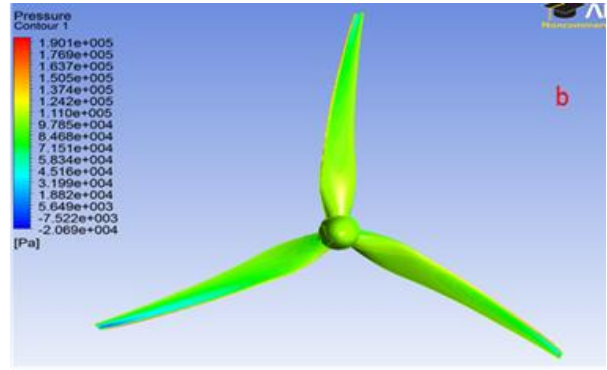
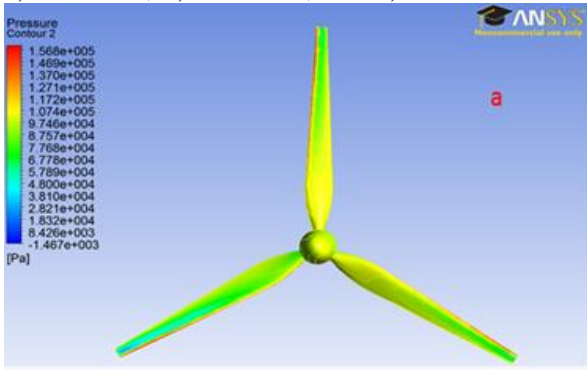
879  
880

**Figure 14 - CB 75% LES-Smagorinsky Convergence Monitoring with Respect to the Defined Convergence Criteria.**



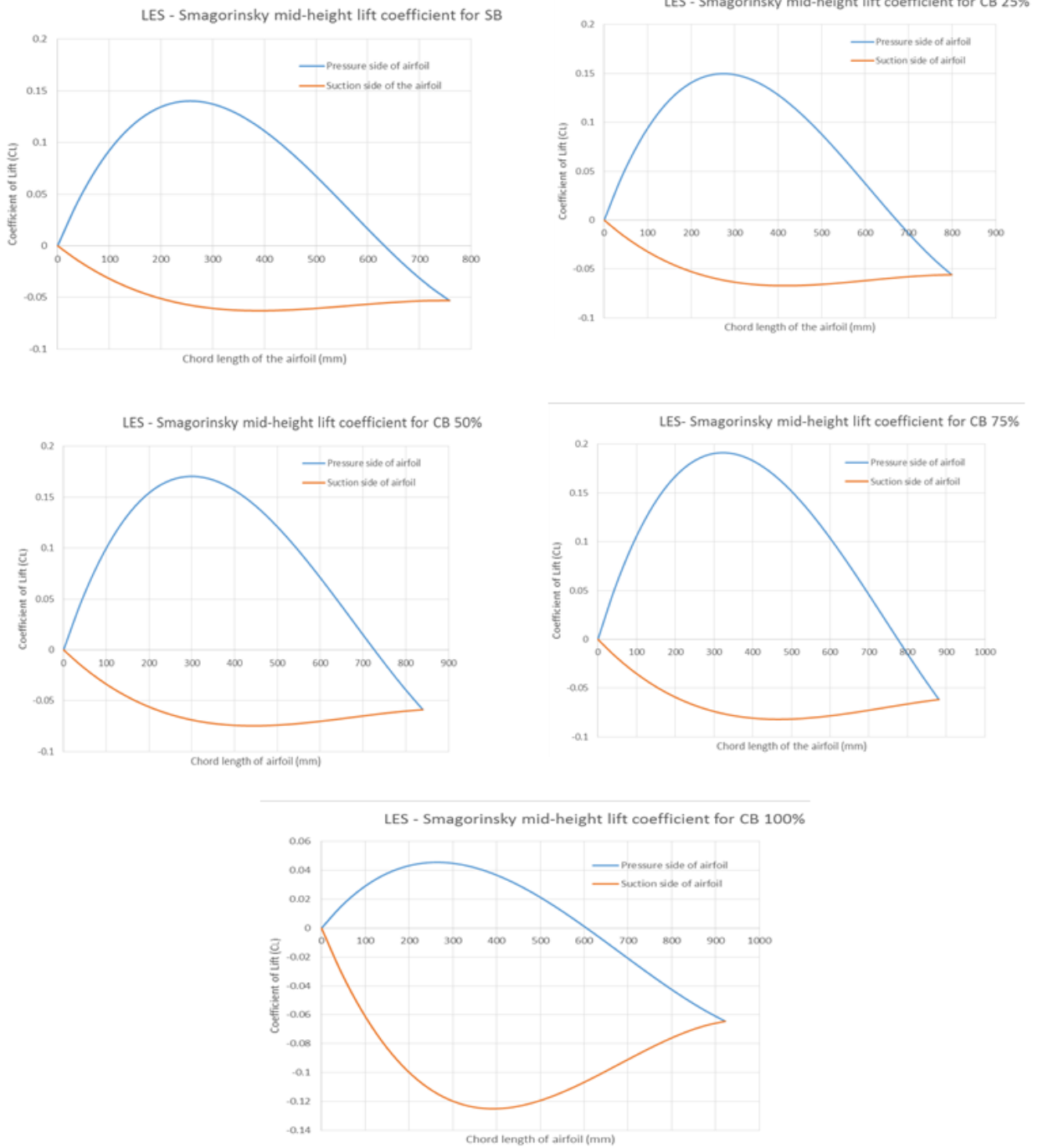
881  
882  
883

884 **Figure 15** – LES-Smagorinsky Blade Pressure Distributions (Pressure Side) on a) SB, b) CB 25 %,  
885 c) CB 50%, d) CB 75%, and e) CB 100%



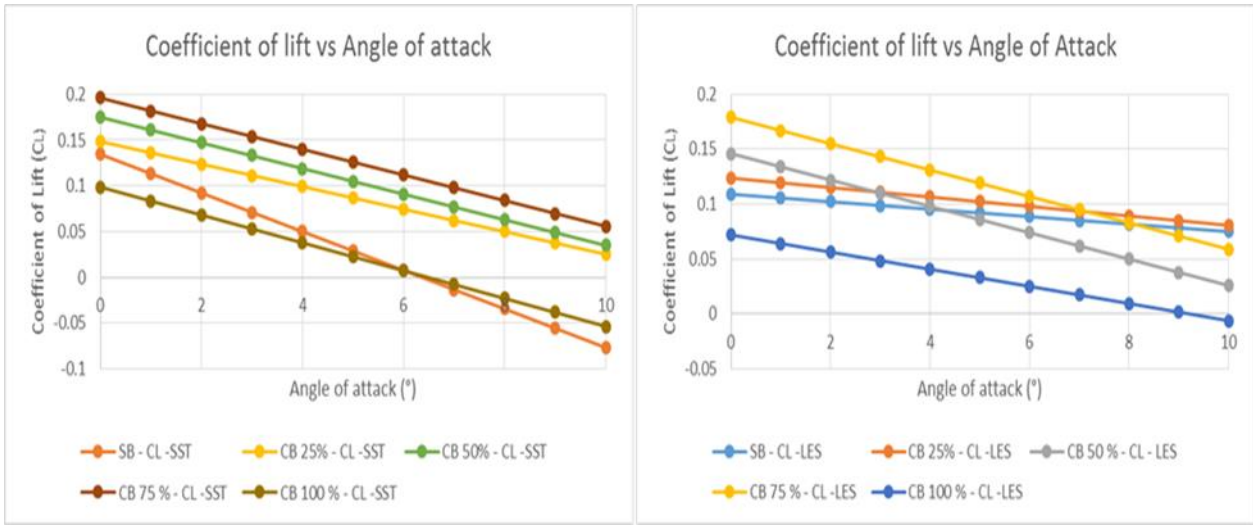
886  
887  
888

889 **Figure 16 - LES – Smagorinsky Mid-height Lift Coefficient Distribution for Five Blade Designs**



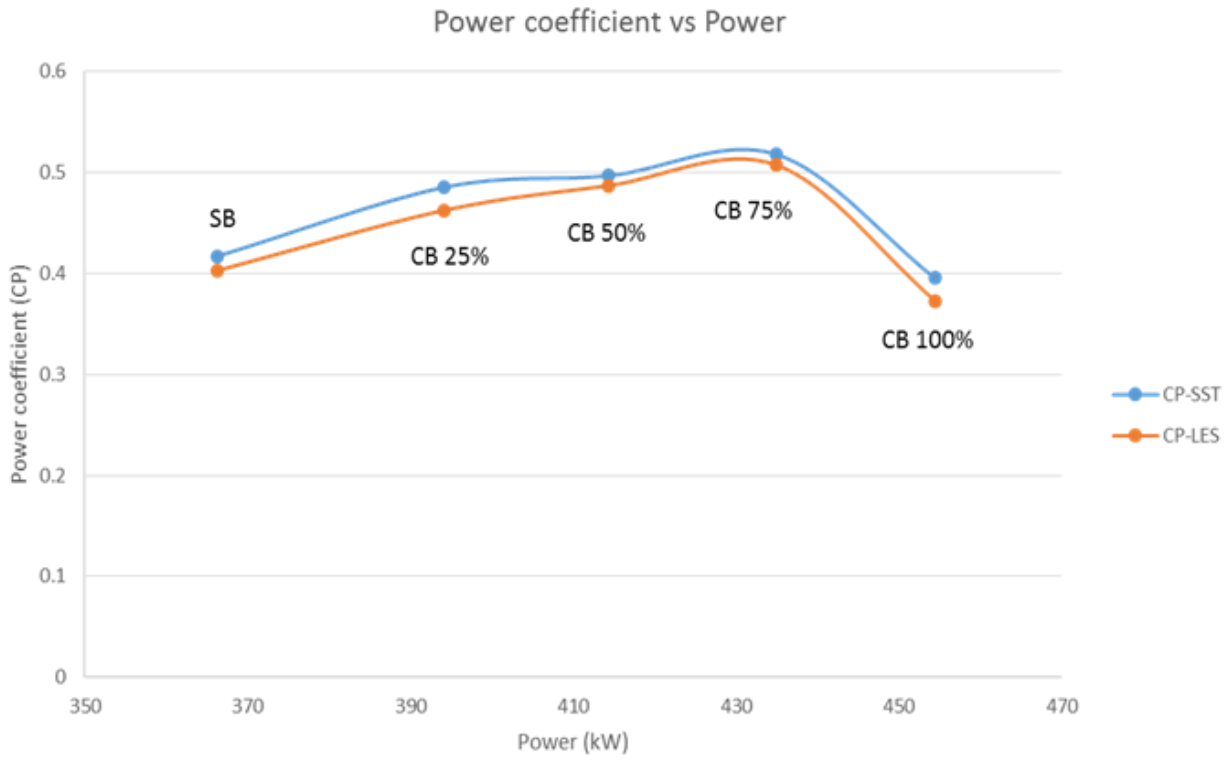
890  
891  
892

893 **Figure 17** - Lift Coefficient Versus Angle of Attack for SST and LES CFD Simulations, at Inlet  
 894 Velocity 2.5m/s  
 895



896  
897

898 **Figure 18** - Power Coefficient Versus Output Power for the Designed Five Blades



899